https://doi.org/10.5194/essd-2022-251
Preprint. Discussion started: 12 August 2022

Open Access Earth System Science Data Discussions

High-resolution and Multitemporal Impervious Surface Mapping in the Lancang-Mekong Basin with Google Earth Engine

Genyun Sun[1,2] , Zheng Li[1], Aizhu Zhang[1], Xin Wang[1], Sunjinyan Ding[1], Xiuping Jia[3], Jing Li[4], Qinhuo Liu [4]

[1] College of Oceanography and Space Informatics, China University of Petroleum (East China), Qingdao, 266580, China
[2]Laboratory for Marine Resources Qingdao National Laboratory for Marine Science and Technology, Qingdao, 266237, China
[3]School of Engineering and Information Technology, The University of New South Wales, Canberra, ACT2600, Australia
[4]State Key Laboratory of Remote Sensing Science, Aerospace Information Research Institute, Chinese Academy of Sciences, Beijing 100101, China

Correspondence to: Aizhu Zhang (zhangaizhu789@163.com)

Abstract. High-resolution and multitemporal impervious surface maps on large scales are crucial for environmental and socioeconomic studies. However, recently available multitemporal impervious surface maps of the Lancang-Mekong basin were limited at 30-m resolution with considerably low accuracy. Hence, the development of up-to-date, accurate, and multitemporal impervious surface maps with the 10-m resolution is urgently needed. In this article, a machine learning framework is demonstrated by fusing Sentinel-1 Synthetic Aperture Radar images and Sentinel-2 Multispectral Sensor images to map and study the annual dynamics of impervious surfaces in the Lancang-Mekong basin from 2016 to 2021 facilitated by Google Earth Engine. Moreover, a train sample migration strategy is proposed to automate impervious surface mapping for various time periods eliminating the need to collect additional train samples from this vast study area. Finally, qualitative and quantitative assessments are conducted using test samples from Google Earth and four existing state-of-the-art datasets. The result shows that the overall accuracy and Kappa of the final impervious surface maps range from 91.45% to 92.44% and 0.829 to 0.848, respectively, which demonstrates the feasibility and reliability of the proposed method and results. The LMISD is freely available from https://doi.org/10.5281/zenodo.6968739 (Sun et al., 2022).

1 Introduction

Impervious surface (IS) is defined as anthropogenic materials, such as roads, roofs, and parking lots, that prevent water from infiltrating into soils (Feng and Fan, 2019; Weng, 2012). IS is an important indicator to understand the human social and environmental impacts of urbanization (Liu et al., 2019). Continuous urban land growth has become a worldwide phenomenon in recent decades, especially in developing countries in Asia and Africa (Liu et al., 2020; Deuskar et al., 2015). Rapid urbanization around the world has brought a series of climate, environmental and social problems, such as biodiversity loss, air pollution, urban heat islands, and urban waterlogging, all of which finally influence the sustainable development of society and human health (Gong et al., 2020; Zeng et al., 2019; Mcdonald et al., 2008). Although urban areas occupy no more than 1%

https://doi.org/10.5194/essd-2022-251
Preprint. Discussion started: 12 August 2022

of the world's land surface, half of the global population now lives on them (Li et al., 2015). Therefore, annual dynamics of high-resolution IS maps can provide quantitative information, which is essential for better understanding the impacts of urbanization and safeguarding urban sustainable development (Xu et al., 2019; Zhu et al., 2019; Gong et al., 2019a; Shao et al., 2016).

Currently, satellite remote sensing offers unique advantages for regional and even global IS mapping due to the frequent revisiting cycles, wide coverage, and low cost. In the past 40 years, many studies on IS or urban area mapping have been conducted based on remote sensing images at different scales and resolutions (Yang et al., 2003; Slonecker et al., 2001; Elvidge et al., 1997; Bian et al., 2019). For example, Zhao (Zhao et al., 2020) mapped urban dynamics in Southeast Asia from 1992 to 2018 using nighttime light (NLT) data from Defense Meteorological Satellite Program (DMSP) and Visible Infrared Imaging Radiometer Suite (VIIRS) with a 1-km resolution. Schneider (Schneider et al., 2010) used ensemble decision trees to extract urban areas from multitemporal 500-m MODIS data. Since 2008, all Landsat archived data have been freely available to the public. Landsat series imagery has become the mainstream data for IS mapping due to its long duration (nearly 40 years) of providing available data with relatively high spatial resolution (30 m). Many regional or global land use and land cover maps with a resolution of 30 m or higher have been produced based on Landsat data (Li et al., 2015; Gong et al., 2019a; Song et al., 2016). GloableLand30 is a representative global land cover product produced by combining pixel-based classification, object-oriented segmentation, and manual editing (Chen et al., 2015) in which IS was regarded as an independent land-cover type. Li and Gong (Li and Gong, 2016) developed an “exclusion-inclusion” framework to extract human settlements at the country level from Landsat imagery. Pesaresi (Pesaresi et al., 2016) used the symbolic machine learning method to obtain a 30-m global human settlement layer (GHSL) based on multitemporal Landsat imagery.Liu (Liu et al., 2018) proposed the normalized urban area composite index (NUACI) via an index-based approach using multitemporal Landsat and NTL data for global urban land mapping. These products have been instrumental in regional climate monitoring, and urban environmental protection. Still, the cloudy and rainy climate in tropical and subtropical areas has seriously affected the quality of optical images, resulting in the accuracy of these products not being enough to meet the actual demand.

Copious studies have shown that the fusion of multisource and multitemporal remote sensing data can improve the IS identification significantly (Shao et al., 2016; Zhang et al., 2020; Salentinig and Gamba, 2015). Compared with optical images, synthetic aperture radar (SAR) images are virtually unaffected by weather conditions, and are more sensitive to the geometric structure and electrical properties of ground objects (Zhang and Xu, 2018; Carrasco et al., 2019). SAR data thus provide complementary information about land properties to improve the IS estimation (Zhang and Xu, 2018). For instance, Lin (Lin et al., 2020) mapped the dynamics of IS in China from 2015 to 2018 by fusing Landsat, Sentinel-1, and NLT data. Zhang

https://doi.org/10.5194/essd-2022-251
Preprint. Discussion started: 12 August 2022

(Zhang et al., 2020) extracted IS at the global level with a random forest (RF) classifier based on SAR polarization scattering characteristics, and multitemporal spectral and texture features from Landsat and Sentinel-1 imagery. Since 2016, the Sentinel-1 and Sentinel-2 data have become freely accessible. They provide C-band SAR imagery and MSI imagery both with a 10-m spatial resolution, which is useful for mapping IS with more spatial details (Xu et al., 2020; Grabska et al., 2020; Dong et al., 2020).

In addition, Google Earth Engine (GEE), a cloud-based platform for processing remote sensing big data, provides all Sentinel-1/2 archived images since 2016 and integrates many excellent classification algorithms, which offers great potential for fine-resolution mapping and monitoring of land cover or IS on a large scale (Gorelick et al., 2017). Up to now, several 10-m resolution single-temporal land cover products have been produced using Sentinel-2 or Sentinel-1 images based on GEE on the national or global scale. For example, Sun (Sun et al., 2019) extracted urban areas based on Sentinel-2 and Sentinel-1 imagery via the threshold-based method over China. Gong (Gong et al., 2019b)used Sentinel-2 as the main data source to map the 10-m global land cover in 2017 based on a pixel-level supervised classification algorithm. However, the existing studies focus on the extraction of IS in a signal phase (e.g. 1 year), which is difficult to meet the demand for spatiotemporal dynamic monitoring of IS. Moreover, the accuracy of existing IS maps can hardly be guaranteed in the Lancang-Mekong River basin where optical images are seriously polluted by clouds.

In this study, we aim to develop a 10-m-resolution IS mapping approach to produce an accurate multitemporal IS database for the Lancang-Mekong basin (called LMISD). The basin is located in the humid tropical area, with cloudy and rainy days for most of the year. Frequent rainy weather and complex terrain reduce the quality and quantity of optical images. To address these issues, we develop a novel framework to fuse time-series Sentinel-1 and Sentinel-2 images for multitemporal IS mapping. The three main contributions of this work are as follows: (1) proposing an RF-based IS extraction framework within the GEE platform. This framework utilizes Sentinel-1 and Sentinel-2 time-series datasets to extract IS with high accuracy. (2) developing an effective method to migrate train samples to facilitate multitemporal IS mapping. (3) assessing the quality of the multitemporal IS product using ground truth samples and four existing land cover products and analyzing the spatiotemporal dynamics of IS in the Lancang-Mekong basin.

2 Study area and dataset

2.1 Study area

The study area covers five countries in the Lancang-Mekong basin, including Vietnam, Laos, Cambodia, Myanmar and Thailand (Fig. 1a). It lies between 5° 37′ -28°32′ N and 92°6′ E- 108° 4′ E, with an area of approximately 2.13×106

https://doi.org/10.5194/essd-2022-251
Preprint. Discussion started: 12 August 2022

km2. The Lancang-Meigong basin has a complex terrain, ranging from -30 m to 5500 m from north to south (Fig. 1b). In general, the climate of the Lancang-Mekong basin is distinctly monsoon and mostly hot and humid. The climate of the region shows a clear difference between the wet seasons (May-October) and dry seasons (November to April). The average annual precipitation in this region is more than 1,500 mm, and 90% of the precipitation falls in the wet season (Nguyen et al., 2012).

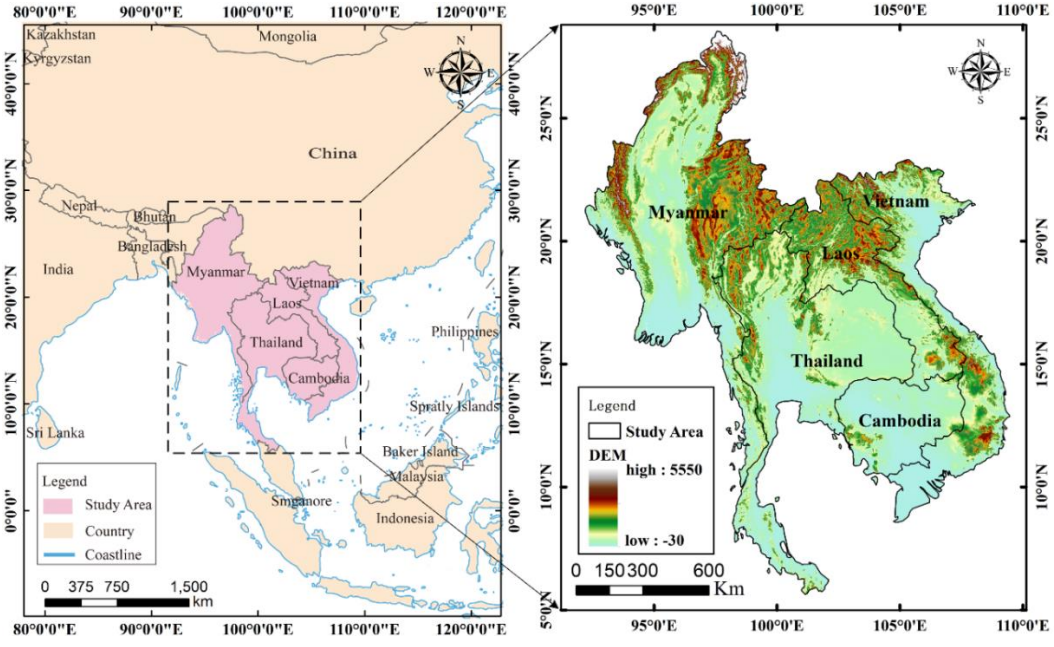

(a) **(b)**

Figure 1: (a) The location of the study area, and (b) its elevation distribution. The administrative boundariy was from China Standard Map Service (http://bzdt.ch.mnr.gov.cn/, last access: 15 January 2022). The DEM imagery was acquired from SRTM 90 m digital elevation data (https://srtm.csi.cgiar.org/, last access: 15 January 2022).

The five countries in the Lancang-Mekong basin are rapidly transforming from rural societies to urbanized societies (Goldblatt et al., 2018). In recent years, the region has undergone a rapid urbanization process. This dramatic urbanization in this region has caused a series of environmental problems, such as water pollution, wetland degradation, and forest destruction (Markert et al., 2018; Ngo et al., 2020). To support addressing these environmental issues, timely, accurate, and fine-resolution IS cover change data are urgently required for relevant studies.

2.2 Datasets and preprocessing

In this article, three kinds of datasets, including 89,536 Sentinel-2 multispectral image blocks and 28,987 scenes of Sentinel-1 SAR GRD images from 2016 to 2021 (Fig. 2), and 1 scene SRTM image, were accessed and processed for the mapping of multitemporal IS across the Lancang-Mekong basin on the GEE platform. Additionally, four existing IS (or land cover)

https://doi.org/10.5194/essd-2022-251
Preprint. Discussion started: 12 August 2022

products were uploaded to the GEE platform for qualitative and quantitative comparison with our results. These data sources are described in detail below.

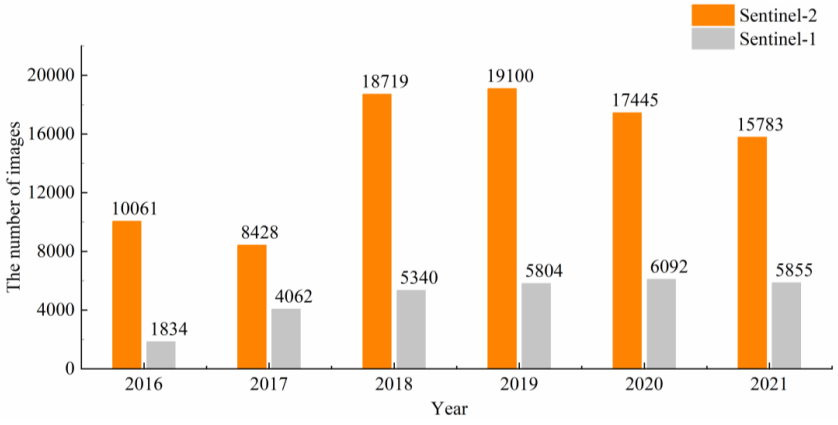

Figure 2: The number of Sentinel-1 and Sentinel-2 images covering the study area from 2016 to 2021.

2.2.1 Sentinel-2 L1C imagery

Sentinel-2 consists of two identical satellites, namely, Sentinel-2A and Sentinel-2B, launched in June 2015 and March 2017, respectively. Sentinel-2 MSI Level-1C images across the five countries from 1 January 2016 to 31 December 2021 were collected for IS mapping in this study. The Sentinel-2 MSI L1C data, which represents the top of atmosphere (TOA) reflectance, contains 13 bands with wavelengths ranging from 443 nm to 2190 nm and spatial resolution ranging from 10 m to 60 m**.** The coastal band (B1), cirrus band (B9), and water vapor band (B10) were sensitive to atmospheric scattering and had a coarse resolution (60 m). Therefore, we used only 10 bands of Sentinel-2 that are important for IS classification. Includes blue, green, red and NIR bands (10 m spatial resolution), and narrow NIR, Red Edge 1-3 and SWIR 1-2 bands (20 m spatial resolution). Then, all 20-m bands were resampled to match the 10-m resolution using nearest-neighbor interpolation. Additionally, cloud cover is a significant consideration in the application of optical remote sensing images. Those images with less than 50% cloud cover were used to ensure sufficient clear pixels on each image. The QA60 (Quality Assessment) band was used to remove the pixels contaminated by clouds and cirrus.

2.2.2 Sentinel-1 SAR GRD

Sentinel-1 A and B satellites provide dual-polarized C-band SAR data with a revisit cycle of 6 days. The sentinel-1 images covering the study area from 1 March 2016 to 1 March 2021 were collected. Among various Sentinel-1 products, the Level-1 Ground Range Detected (GRD) scenes with VV and VH polarization in IW mode operated in an ‘ascending’ or ‘descending’ orbit were used in this study. The 10 m spatial resolution of the GRD images provides opportunities for fine IS mapping. Each GRD image archived on the GEE platform has been preprocessed by the Sentinel-1 Toolbox, including thermal noise removal,

https://doi.org/10.5194/essd-2022-251
Preprint. Discussion started: 12 August 2022

radiometric calibration, and terrain correction. Then, the final terrain correction values were processed to the backscatter coefficient (σ°) in decibels (dB) (https://developers.google.com/earth-engine/sentinel1).

130 **2.2.3 Other auxiliary data**

Numerous previous studies have demonstrated that most IS are distributed in flat terrain areas (Zhang et al., 2020; Lin et al., 2020). The digital elevation model (DEM) data produced by the Shuttle Radar Topography Mission (SRTM) with a resolution of approximately 30 m were utilized as an auxiliary dataset for IS mapping. The slope image obtained from the DEM was used to mask the mountain area.

135 To estimate the accuracy and reliability of our products, four excellent global IS (or land cover) products were compared against ours. These products include based-on Multisource and Multitemporal images IS product (MSMT-2015), Finer Resolution Observation and Monitoring of Global Land Cover product (GLC10-2017), Global Artificial Impervious Areas (GAIA), and European Space Agency WorldCover product (ESA-2020). These state-of-the-art products have their different advantages and characteristics, described in detail below.

140 MSMT-2015 used in this study is derived from the composite Landsat 8 OLI and Sentinel-1 SAR imagery (Zhang et al., 2020). The IS was extracted through RF classifiers along with spectrum, texture, and backscattering features. The product has a spatial resolution of 30 m with an overall accuracy of 96.6%.

GLC10-2017 is an existing global land cover map with a 10-m resolution consisting of 10 categories (Gong et al., 2019b). GLC10-2017 was derived from Sentinel-2 imagery of 2017 based on supervised learning based on RF classifier. Similarly, the

145 IS areas were also extracted from GLC10-2017 as independent land-cover type.

GAIA is an annual map of the global artificial impervious areas between 1985 and 2018 produced using the “Include-exclude” method based on the GEE platform (Gong et al., 2020). Its overall accuracy is reported to be over 90% with a 30-m resolution. In this study, the IS map of 2018 (named GAIA-2018) was employed for comparative analysis.

ESA-2020 is the latest global land cover product at 10 m resolution for 2020, and it was produced using machine learning

150 classification algorithms based on Sentinel-1 and 2 images (Van De Kerchove et al., 2021). It contained 11 land-cover classes. Because the definitions of built-up area and IS are similar, we extracted the ‘build-up’ areas from the land cover map to compare with our results.

https://doi.org/10.5194/essd-2022-251
Preprint. Discussion started: 12 August 2022

3 Methods

As shown in Fig. 3, the proposed method consists of four main parts: (1) the feature extraction (Section 3.1), (2) training samples collection and migration (Section 3.2), (3) multitemporal impervious surface extraction (Section 3.3), and (4) accuracy assessment (Section 3.4). The processing framework was implemented using JavaScript codes on the GEE platform (https://code.earthengine.google.com). Relevant details of these parts are presented as follows.

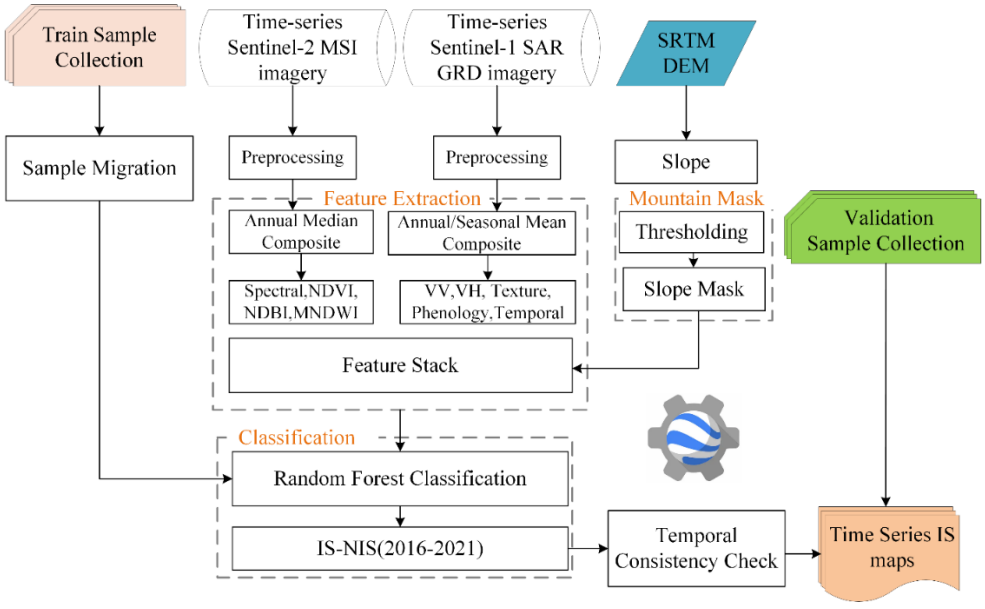

Figure 3: The flowchart of the time series IS mapping.

3.1 Feature Extraction

The performance of classification algorithms depends on the extraction of appropriate features. In this section, the features extracted from optical and SAR datasets are discussed.

3.1.1 Mosaic and spectral feature extraction for optical images

Spectral features play an important role in accurately identifying IS because they reflect the physical spectral characteristics of ground objects (Priem et al., 2019). The Lancang-Mekong River basin is located in the tropical monsoon climate zone, and the complex climatic conditions seriously affect the quality of optical images. Therefore, after masking out the bad pixels (such as clouds, shadows, and saturated pixels), the annual median aggregations were generated. Specifically, if there were multiple images in the same location within a year, the pixel with the intermediate value was used as representative data of the year.

https://doi.org/10.5194/essd-2022-251
Preprint. Discussion started: 12 August 2022

Median aggregations have the effect of removing noisy, extremely dark or bright pixels that may be caused by scene-specific illumination conditions, such as shadow and haze (Gong et al., 2019b).

Additionally, several spectral indices can enhance the difference in spectral properties between IS and other ground objects. Table 1 lists the three popular spectral indices used in the study. They are combined with the original spectral bands of Sentinel-2 images as optical features input into the classifier.

Table 1: Spectral indices derived from Sentinel-2 imagery.

Indices	Abbreviation	Equations
Normalized Differential Vegetation Index	NDVI	$\frac{B8-B4}{B8+B4}$
Normalized Differential Built-up Index	NDBI	$\frac{B11-B8}{B11+B8}$
Modified Normalized Differential Water Index	MNDWI	$\frac{B3-B11}{B3+B11}$

3.1.2 Backscatter-temporal-texture feature extraction from SAR data

SAR features show geometric properties via scattering characteristics, which can provide valuable information to complement and enhance multispectral observations for IS mapping. The mean values of all VV and VH time-series images within each year were calculated (named Y_VV and Y_VH). The advantage of mean aggregation is that it can reduce the influence of layover, speckle noise, and shadows (Quin et al., 2014). Moreover, the annual standard deviation of the VV and VH imagery (named VV_Stddev and VH_Stddev) was directly derived from all GRD images available for each year to capture the temporal metrics of objects.

Furthermore, artificial IS generally remains stable for a short period (e.g., 1 year), while natural objects, especially crops and vegetation, usually change with seasons and climate. Thus, phenological information is useful for separating IS from other land cover types effectively. According to the climate change in the Lancang-Mekong basin, the time-series Sentinel-1 images available each year were divided into four groups based on the seasons. Then, a mean function was applied to each group, calculating the mean at the pixel level correspondingly, resulting in eight phenological metrics of backscattering for each year (named VV_t, VH_t, t = 1,2,3,4, t represents the seasons).

In addition, as texture features are effective for highlighting the local spatial characteristics of different land-cover types (Ansari et al., 2020), we calculated five texture variables for each annual mean aggregated VV and VH image (Y_VV and Y_VH) based on the gray-level co-occurrence matrix (GLCM) method. The five texture variables include angular second moment (ASM), entropy (ENT), inverse difference moment (IDM), Correlation (CORR), and sum average (SAVG), which

https://doi.org/10.5194/essd-2022-251
Preprint. Discussion started: 12 August 2022

have been proven to be effective in the mapping of IS (Zhang et al., 2016; Uhlmann and Kiranyaz, 2014). Notably, the optimal window size for texture measurements is intimately related to the image spatial resolution and land-cover distribution. According to the research of (Puissant et al., 2005), we calculated the texture measures from the average of the directional bands within a 7x7 window.

Finally, ten spectral features and 3 index features from the Sentinel-2 imagery, 2 annual mean of backscattering, 8 topographical features, 2 temporal metrics, and 10 texture features from Sentinel-1 imagery, were stacked, producing a single multidimensional image with 35 layers over the study area (Table 2). Here they were used in classification algorithms for mapping IS.

Table 2: Data sources and training features used in this study

Data	Features	Number
Sentinel-2 Optical	Spectral features: median composition of B2, B3, B4, B5, B6, B7, B8, B8A, B11, B12	10
	Normalized indices: NDVI, NDBI, MNDWI	3
Sentinel-1 SAR	Backscattering: annual mean of VV, VH time-series image	2
	Phenological metrics: seasonal mean of VV, VH time-series image	8
	Temporal metrics: standard deviation of VH, VV	2
	Textural features: angular second moment (ASM), entropy (ENT), inverse difference moment (IDM), Correlation (CORR) and sum average (SAVG) of each seasonal mean of VV and VH	10

3.2 Train sample collection and migration

The vast territories of the study area require numerous training samples to ensure the classification accuracy. To obtain sufficient and representative samples with time and cost savings, we adopted the random clustered sampling technique (Stehman and Foody, 2019a) to randomly allocate 2920 sample polygons across the Lancang-Mekong basin. Each sample polygon contained approximately 10 random points. The distance between each sample point was at least 30 m to obtain the representativeness of each land cover type and avoid autocorrelation. Altogether, 9107 IS samples and 17910 NIS samples were obtained for 2016. The IS sample contains as many materials as possible, such as buildings, roads, etc., while the NIS sample contains vegetation, water, and soil (Table 3). Google Earth high-resolution images were used as references to identify land cover types.

https://doi.org/10.5194/essd-2022-251
Preprint. Discussion started: 12 August 2022

Table 3: Number of train samples collected for classification in 2016.

Class	SubClass	Sample Polygons	Samples Points
IS	IS	974	9107
NIS	vegetation	562	4739
	soil	755	7205
	water	629	5966

Considering the cost and practical issues, it is very difficult to obtain consistent and high-quality training samples every year, especially in large scale IS mapping (Huang et al., 2020). Also, due to the continuous land cover conversion by human activity and phenological change, directly using ground truth samples acquired from the reference year to classify images from other years is inappropriate. Therefore, we developed an efficient method to migrate high-quality train samples to another year (i.e., target year) for IS mapping over different time intervals without collecting ground truth each time. Fig.4 illustrates the flowchart of the proposed method.

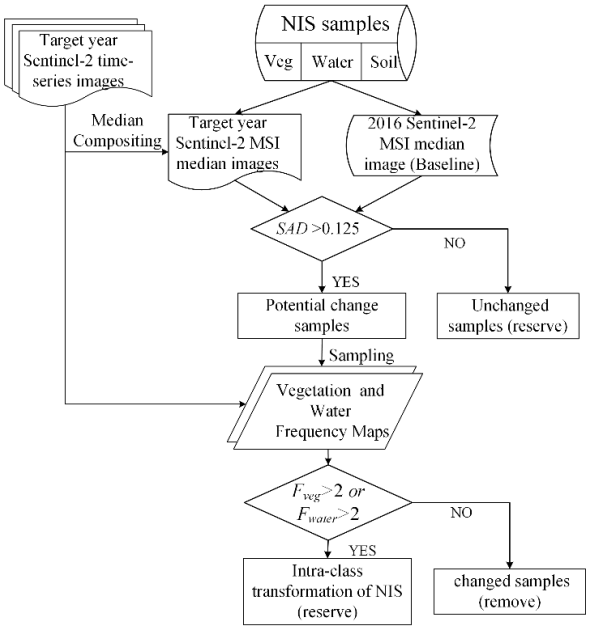

Figure 4: The flowchart of the proposed automatic training sample migration method.

On the basis of Schneider's research(Schneider and Mertes, 2014), the change process from NIS to IS can be reasonably assumed to be irreversible in a short duration. Therefore, the NIS training samples selected in 2016 may change to IS in the later years, while the labels of IS samples in 2016 are assumed to remain as IS during the study period. We address the cases where the NIS type converted to IS due to urbanization in the training sample migration method. We divided NIS samples with

https://doi.org/10.5194/essd-2022-251
Preprint. Discussion started: 12 August 2022

label changes into two categories, intra-class changes for the NIS (i.e. inter-transformation of vegetation, bare land, and water bodies) and NIS-to-IS category transformations. Since in binary classification tasks, the intra-class changes for the NIS have little effect on the classification results. Thus, we mainly focus on the samples transformed from NIS to IS. The proposed method consists of three main steps: (1) at a given reference sample location, one label was interpreted based on the Sentinel-2 and Google Earth images acquired in the beginning year (e.g., 2016). The spectra extracted from the beginning year are considered the reference spectra, and the other years' spectra are considered the target spectra. (2) For those NIS samples, the spectral angular distance (SAD) between the reference spectra and target spectra were calculated using Eq. (1). The SAD allows the amount of real change between the reference spectra and target spectra to be measured. Afterward, a thresholding of 0.125 was set to determine the train samples with a high probability of experiencing landcover changes. Non-change pixels have remained as the training samples for NIS for the current year. (3) The frequencies of water (F_{water}) and vegetation ($F_{vegetation}$) at the sample points were counted using Sentinel-2 time-series images in the target year. The NIS samples whose F_{water} or $F_{vegetation}$ greater than 2 will be considered to have undergone only intra-class changes. The formulas of F_{water} and $F_{vegetation}$ are shown in Eq (2) to Eq (5). Finally, the number of samples identified as having no change for each year is listed in Table 4.

$$SAD = \cos^{-1}\left(\frac{X^{0^T} X^t}{\sqrt{X^{0^T} X^t}\sqrt{X^{t^T} X^0}}\right) \quad (1)$$

Where X^0 is the reference spectra when the ground truth samples were collected in 2016, and X^t is the target spectra at time $t(t = 2017, 2018, ..., 2021)$

$$water = \begin{cases} 1 & MNDWI > 0.12 \\ 0 & other\ values \end{cases} \quad (2)$$

$$F_{water} = \frac{\sum N_{water}}{\sum N_{total}} \quad (3)$$

$$vegetation = \begin{cases} 1 & NDVI > 0.25 \\ 0 & other\ values \end{cases} \quad (4)$$

$$F_{vegetation} = \frac{\sum N_{vegetation}}{\sum N_{total}} \quad (5)$$

https://doi.org/10.5194/essd-2022-251
Preprint. Discussion started: 12 August 2022

Where $\sum water$ and $\sum vegetation$ represent the number of water and vegetation pixels calculated using Eq. (2) and Eq. (4), $\sum total$ is the number of good quality pixels.

Table 4: The number of train samples identified as no change for each year

Class	Subclass	2016	2017	2018	2019	2020	2021
NIS	soil	7205	5658	6108	6003	5953	5534
	vegetation	4739	4054	4029	3940	3699	3550
	water	5966	5937	5938	5935	5916	5904
IS	IS	9107	9107	9107	9107	9107	9107

3.3 Multitemporal impervious surface extraction

3.3.1 Classification on GEE

The GEE platform provides many supervised classifiers, including the naive Bayes classifier, CART, maximum likelihood classifier (MLC), support vector machine (SVM), and RF, etc. Among these classifiers, RF already demonstrates massive potential for large-scale IS extraction (Lin et al., 2020). The RF classifier is an ensemble classifier composed of many decision trees, and each tree is grown using randomly selected training samples and features based on the bootstrap aggregation technique (Breiman, 2001). The final class is determined by the majority of votes from all decision trees. RF exhibit more robustness to variations in input data and less sensitive to mislabeled training data or overfitting. RF has two parameters: the number of trees (Ntree) and the number of variables split at each tree node (Mtry). Here, taking into account the computational efficiency and on the basis of trial and error, Ntree was set as 500, Mtry was set as the square root of the number of input variables, and the other parameters remained the default. In this study, the RF classifiers were separately trained for each year of IS classification in the Lancang-Mekong basin. Within each year, the migrated train samples were used to save labor costs and reduce the influence of label noise on classification. The input features are listed in Table 2.

Bare rock in mountainous areas has similar spectra and backscattering with urban buildings, which can result in obvious misclassification. Before classification, DEM data were used to calculate slope. Pixels with a slope greater than 15° were labeled as NIS.

https://doi.org/10.5194/essd-2022-251
Preprint. Discussion started: 12 August 2022

Additionally, in pixel-based classification, the classification map may show a salt-and-pepper noise. Considering that IS in rural and suburban areas are usually small, spatial filtering with a 3 ×3 window was employed to reduce the effect of "salt and pepper" based on a "majority vote" rule.

3.3.2 Temporal consistency check

In multitemporal IS mapping, due to misclassification, the initial IS sequence may not conform to the irreversibility assumption. To generate more credible and reliable IS sequences, a temporal consistency checking method is presented in this section, which includes two parts: temporal filtering and consistency check (Fig. 5). Temporal filtering is designed to remove the noise (or misclassification) caused by individual classifications. Detailed procedures of temporal filtering are shown in Fig. 5a. For each pixel C_{ij}^{t} (i.e., t represents a specific year and i, j represents the pixel position), a temporal sliding window of size Tw $Tw(Tw=2k+1, k=1,2...)$ was employed to determine its final label by majority voting. Then, with a gradual increasing of the temporal window size Tw, the filtering procedure will be implemented again until the labels of all pixels in the sequence no longer change. This ensures that the classification results are similar for adjacent years.

Although most misclassification noises in the initial sequence can be modified by temporal filtering, the sequence may still contain unreasonable class conversion (form IS to NIS). For this reason, a consistency check process was implemented based on two following steps: (1) Reverse traverse the sequence from 2016 to 2018. If the pixels in the next three years are all NIS, the pixel in the current year will be set to the NIS. (2) Forward traversal the sequence from 2019 to 2021. If the previous three years are all IS, then the pixel in the current year will be set as the IS. The details of the consistency check are represented in Fig. 5b.

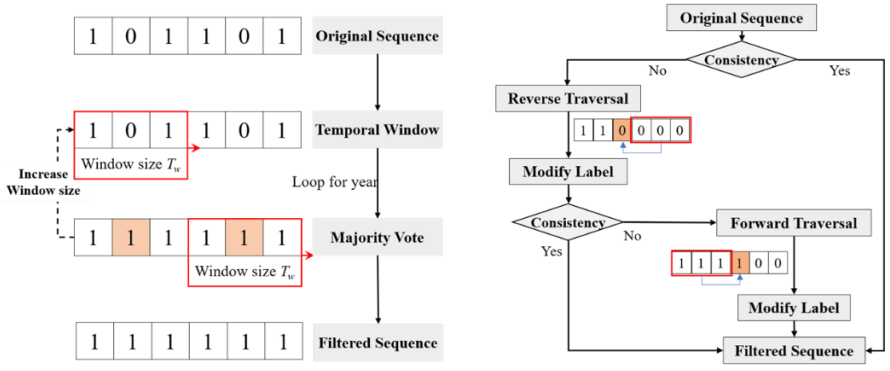

(a) (b)

Figure 5: The proposed temporally consistent check process: (a) temporal filter, (b) consistency check. (1 for IS, 0 for NIS).

https://doi.org/10.5194/essd-2022-251
Preprint. Discussion started: 12 August 2022

3.4 Accuracy assessment

Accurate assessment requires sufficient test samples for both NIS and IS. In this study, we took the stratified random sampling strategy to obtain 9792 (4765 for IS and 5027 for NIS) independent test samples for 2016. Since the extraction results of IS in other years were generated using migrated training samples, we acquired 9851 (4592 for IS and 5259 for NIS) test samples using the same sampling strategy in 2021 to verify the accuracy of our products and the effectiveness of sample migration. The sample interpretation was based on Google Earth images and Sentinel-2 images. Fig.6 depicts the test sample distribution in the study area for 2016 and 2021.

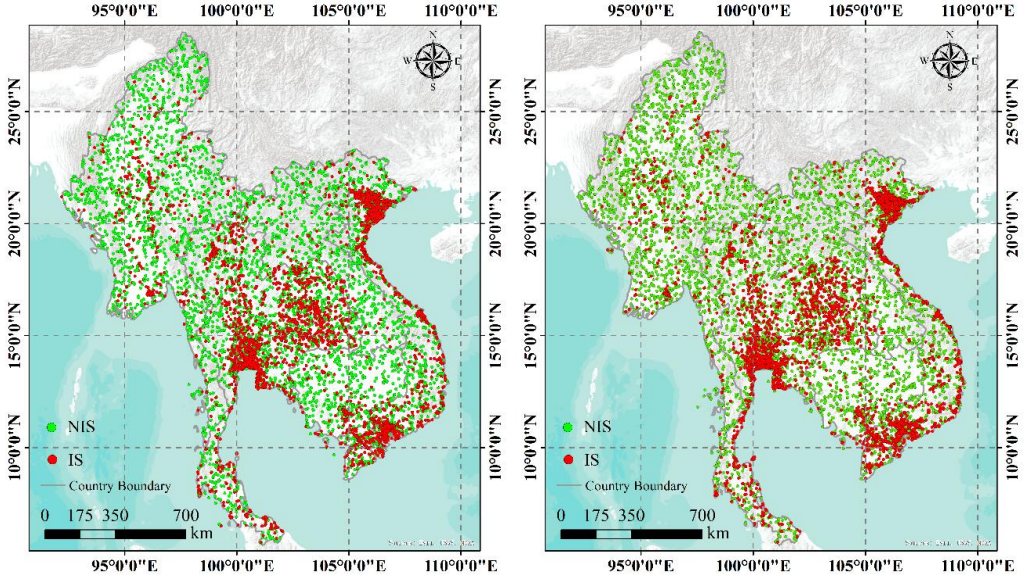

Figure 6: The spatial distribution of the test samples, (a) test samples for 2016, (b) test samples for 2021. The background imagery is the World Hillshade from Esri (http://goto.arcgisonline.com/maps/Elevation/World_Hillshade, last access: 15 January 2022). The administrative boundariy was from China Standard Map Service (http://bzdt.ch.mnr.gov.cn/, last access: 15 January 2022).

The confusion matrix of the IS maps was calculated to evaluate the accuracies of the results based on test samples. Four accuracy indices, including the OA, UA, PA, and Kappa, were obtained. The OA and Kappa provide a total perspective of IS extraction performance. PA indicates the consistency between the reference data and the classification, while UA evaluates the consistency of the classified pixels with the known reference data. UA and PA are related to commission error and omission error, respectively (Stehman and Foody, 2019b).

Additionally, the test samples from 2016 were used to evaluate the accuracy of GLC10-2017, MSMT-2015, and GAIA-2018, and test samples from 2021 were obtained to evaluate the accuracy of ESA-2020 in the Lancang-Mekong basin. Moreover,

https://doi.org/10.5194/essd-2022-251
Preprint. Discussion started: 12 August 2022

four representative regions with different impervious landscapes were selected to further visually compare the differences between our products and the four state-of-the-art land-cover products.

4 Result

4.1 Spatiotemporal patterns of impervious surfaces

As shown in Fig.7, the derived IS maps of the Lancang-Mekong basin provide accurate information about the distribution of IS areas. Large continuous IS are mostly in the eastern and southern coastal areas, which are closely related to the convenient land and sea transportation in these areas and the relatively high level of economic development. Conversely, the impervious areas in the northern part of the Lancang-Mekong basin are fragmented and tiny, owing to the complex and rugged mountains distributed in this region. Fig.8 shows enlarged views of two typical regions. As shown, the multitemporal IS maps are consistent with the real ground cover and reflect the IS dynamic information accurately. With the advantages of high spatial resolution, furthermore, the fine structure of urban space, such as urban roads, bare land, and small rivers, can be accurately identified (white and purple ellipses in Fig.8).

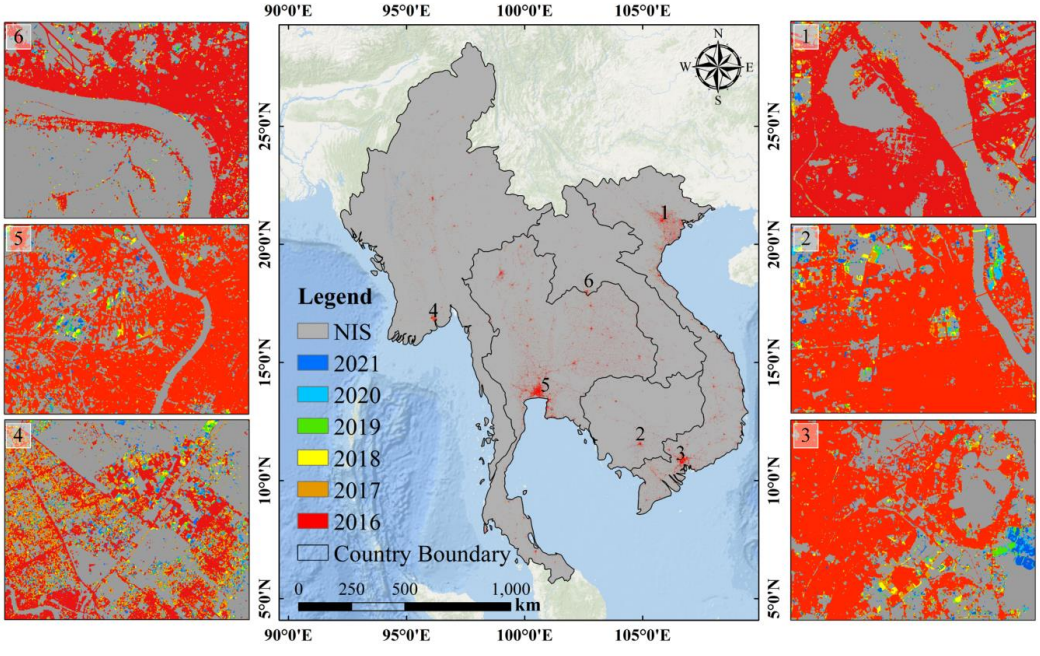

Figure 7: The resultant temporal IS expansion map in the Lancang-Mekong basin (2016–2021). The base map was the Ersi World Ocean Base Map (http://goto.arcgisonline.com/maps/World_Ocean_Base, last access: 15 January 2022). The administrative boundariy was from China Standard Map Service (http://bzdt.ch.mnr.gov.cn/, last access: 15 January 2022).

https://doi.org/10.5194/essd-2022-251
Preprint. Discussion started: 12 August 2022

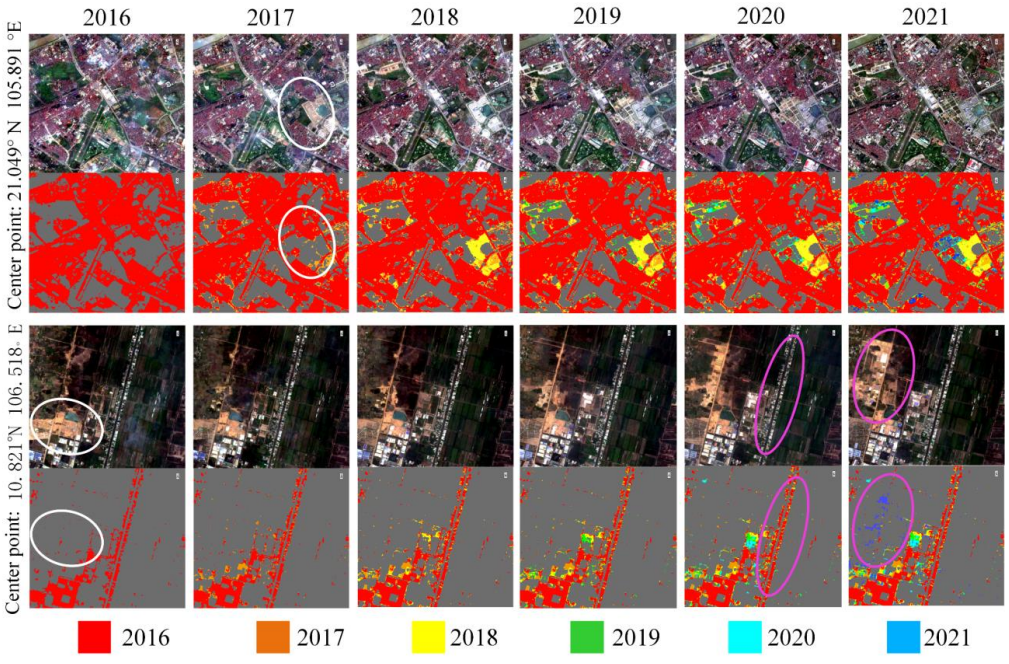

Figure 8: Visual comparison between Sentinel-2 images and IS mapping results. The Sentinel-2 images, comprised of red, green and blue bands, was from European Space Agency (https://sentinel.esa.int/web/sentinel/missions/sentinel-2, last access: 03 January 2022).

Fig.9 presents that the Lancang-Mekong basin had experienced an unprecedented urban sprawl process from 2016 to 2021. Statistically, over the Lancang-Mekong basin, the IS area was 22817.87 km^2 in 2016 and increased to 37220.27 km^2 in 2021 (Fig.9 a). On the national scale, Thailand has the biggest IS area from 11017.69 km^2 in 2016 to 15927.42 km^2 in 2021. By contrast, Vietnam has the most significant expansion of IS area, with an average growth rate of 831.67 km^2/year, from 7946.81 km^2 in 2016 to 12936.79 km^2 in 2021. Following these three countries are Myanmar (i.e., from 2120.15 km^2 in 2016 to 5349.80 km^2 in 2021), Cambodia (i.e., from 988.18 km^2 in 2016 to 1747.02 km^2 in 2021), and Laos (i.e., from 745.04 km^2 in 2016 to 1259.24 km^2 in 2021).

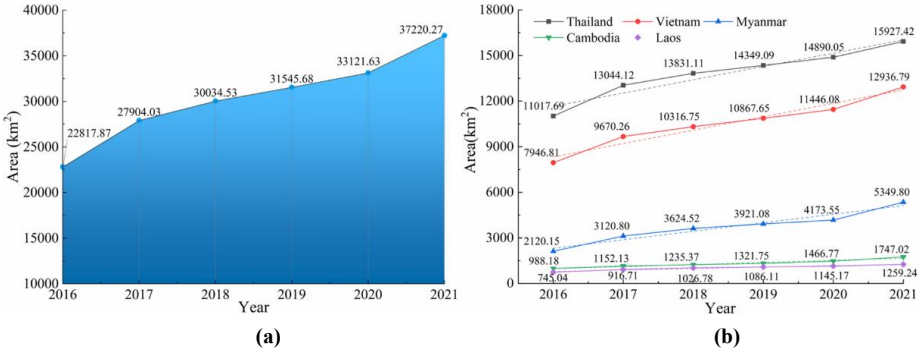

Figure 9: IS area in the Lancang-Mekong River basin and five countries.

https://doi.org/10.5194/essd-2022-251
Preprint. Discussion started: 12 August 2022

Fig.10 and Fig.11 show the meridional and zonal total IS area for each of the 0:05° longitude and latitude intervals. In the zonal statistics (Fig. 10) result, we found that 90% of the IS are distributed between 10° and 22° N because most developed cities are located in those regions. The three peaks in the zonal direction are located in the centers of Ho Chi Minh City, Bangkok, and Hanoi. The meridional results (Fig.11) reveal that there are three peak intervals: 96° E to 96.5° E (Myanmar), 99° E to 101° E (Thailand), and 105° E to 107° E (Eastern Cambodia and Vietnam). It is worth noting that the region with a larger IS area, regardless of longitude or latitude, has a larger increase in IS area from 2016 to 2021.

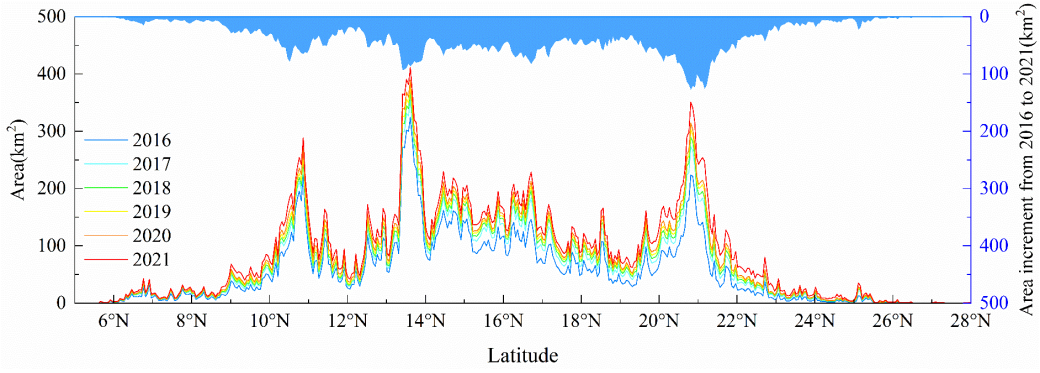

Figure 10: The distribution of IS area and increasement calculated at 0.05 ˚interval along the latitude from 2016 to 2021.

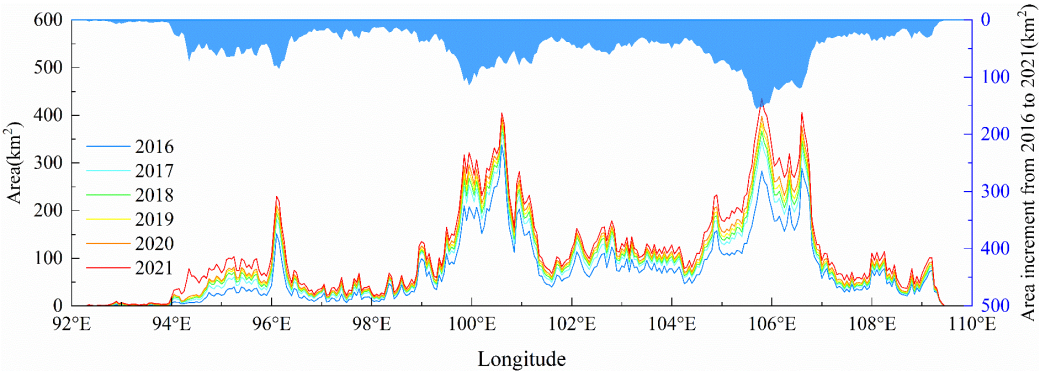

Figure 11: The distribution of IS area and increasement calculated at 0.05 ˚interval along the longitude from 2016 to 20121.

4.2 Accuracy assessment of the IS mapping

4.2.1 Accuracy assessment using test samples

The accuracy of the six IS maps over five countries and the entire Lancang-Mekong basin is presented in Table 5. Overall, LMISD-2016 achieves the highest OA and Kappa of 92.44% and 0.848, respectively.

https://doi.org/10.5194/essd-2022-251
Preprint. Discussion started: 12 August 2022

Table 5: Accuracy assessment between different datasets based on test samples.

		Vietnam	Laos	Cambodia	Myanmar	Thailand	overall
LMISD-2016	UA	94.85	77.24	90.45	87.72	95.13	93.76
	PA	91.11	88.89	88.75	90.24	90.22	90.45
	OA	**91.06**	**93.09**	**94.50**	**95.30**	**91.01**	**92.44**
	Kappa	**0.808**	**0.824**	**0.861**	**0.8596**	**0.812**	**0.848**
LMISD-2021	UA	91.46	74.29	71.20	76.78	88.69	87.70
	PA	94.49	88.64	90.07	95.70	95.87	94.99
	OA	**90.56**	**94.55**	**91.49**	**94.73**	**90.12**	**91.45**
	Kappa	**0.787**	**0.776**	**0.713**	**0.820**	**0.789**	**0.829**
ESA-2020	UA	90.56	74.56	75.63	75.29	88.37	87.26
	PA	96.51	96.59	98.68	93.41	95.96	96.08
	OA	**91.08**	**95.02**	**91.50**	**94.08**	**89.93**	**91.63**
	Kappa	**0.796**	**0.814**	**0.797**	**0.798**	**0.785**	**0.833**
GLC10-2017	UA	96.17	94.64	96.08	91.35	97.75	96.47
	PA	69.43	42.06	61.25	53.88	61.81	63.24
	OA	**78.47**	**88.66**	**89.47**	**89.22**	**75.26**	**81.01**
	Kappa	**0.578**	**0.528**	**0.686**	**0.618**	**0.530**	**0.616**
MSMT-2015	UA	96.25	93.55	93.83	92.25	96.05	96.57
	PA	78.56	69.04	47.50	51.29	64.75	76.87
	OA	**84.17**	**93.28**	**85.81**	**91.77**	**92.02**	**87.51**
	Kappa	**0.678**	**0.756**	**0.554**	**0.617**	**0.737**	**0.754**
GAIA-2018	UA	98.19	83.02	98.36	99.13	98.05	98.12
	PA	47.99	34.92	37.50	25.50	43.36	42.90
	OA	**65.84**	**86.41**	**83.89**	**84.26**	**64.09**	**71.86**
	Kappa	**0.383**	**0.465**	**0.4681**	**34.96**	**0.354**	**0.428**

345

https://doi.org/10.5194/essd-2022-251
Preprint. Discussion started: 12 August 2022

ESA-2020 obtains the second highest accuracy with OA and Kappa of 91.63 % and 0.833, which is slightly better than the accuracy of our results in 2021 (LMISD-2021). Considering that LMISD-2021 is obtained using migrated training samples, it still maintains similar accuracy to ESA-2020, which demonstrates the reliability and stability of our products, as well as the effectiveness of sample migration. In contrast, the OA of the other three IS products is less than 90%, and the Kappa is less than 0.8.

Concerning the PA of the IS class, ESA-2020 performs best and achieved a PA of 96.08%, followed by the LMISD-2021 value of 94.99%, and the LMISD-2016 value of 90.45%. An explanation for this might be that the application of SAR data enhances the separability of IS and other types partly, thus reducing the omission of small and fragmented impermeable objects. By contrast, the PA values of GLC10-2017, MSMT-2015, and GAIA-2018 are all less than 80%. From the perspective of the UA for IS, GAIA-2018 has the best performance in UA (98.12%), but its low PA (42.90%) implies the apparent omission errors of IS. The UA values of GLC10-2017, MSMT-2015, ESA-2020 are 96.47%, 96.57%, separately. Compared with PA of IS, these reference products had better performance on the UA metrics, which demonstrates they have a lower commission error.

Furthermore. the accuracy of IS varies significantly in different countries. Generally, the accuracy of our results is higher in Vietnam and Thailand, which have larger IS areas. Above all, a satisfactory quality of the final IS sequence is achieved. We are confident that our products can be further applied to practical applications in IS analyses in the Lancang-Mekong basin.

4.2.2 Comparison with other products

Four representative scenarios were selected for detailed analysis to compare the differences between our results and existing four intuitively IS products. As shown in Fig.12, these scenarios were displayed in the historical Sentinel-2 RGB image (2016), LMISD-2017, ESA-2020, GLC10-2017, MSMT-2015, and GAIA-2018 products. Columns (a) depict the urban area (Bangkok), which were chosen to represent the holistic performance of different products in the description of urban areas with dense buildings. The details of suburb areas surrounding a large amount of bare land and farmland are displayed in column (b). Columns (c) and (d) show rural areas with sparse buildings and mountain areas surrounded by large amounts of rock and bare soil, respectively.

https://doi.org/10.5194/essd-2022-251
Preprint. Discussion started: 12 August 2022

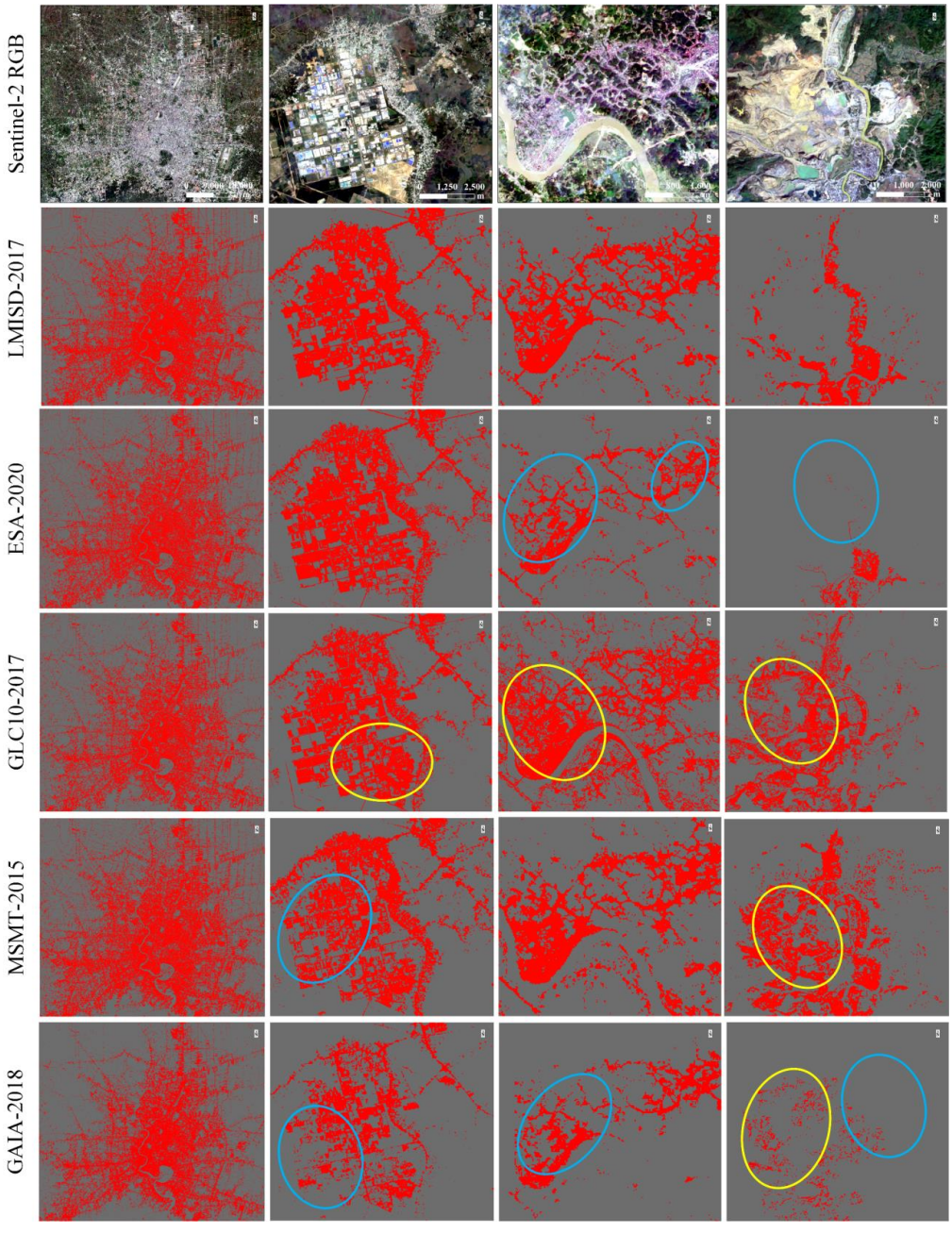

Figure 12: Comparisons between the LMISD and other products. The Sentinel-2 images in the first row, comprised of red, green and blue bands, was from European Space Agency (https://sentinel.esa.int/web/sentinel/missions/sentinel-2, last access: 03 January 2022). In rows 2-6 of the figure, the red area represents the IS and the gray area refers to the NIS. The blue ellipse highlights the omission region and the yellow ellipse represents the commission region.

https://doi.org/10.5194/essd-2022-251
Preprint. Discussion started: 12 August 2022

Generally , all products provide good consistency with ground truth in urban areas and can accurately reflect the surface conditions. However, there were subtle differences among those products in suburbs, rural, and mountain areas. Of all 10-m IS maps, our result (LMISD-2017) is most consistent with ESA-2020, but ESA-2020 ignores spars buildings in rural and mountainous areas, resulting in slight IS underestimation (row3, blue ellipses). By contrast, most bare land, sand, and rocks were wrongly classified as IS in GLC10-2017 in suburbs and rural areas (row 4 yellow ellipses). LMISD-2017 provides relatively satisfactory IS extraction results in all scenarios, especially for the buildings with tiny sizes in rural and mountain areas.

Among the 30-m land cover products (rows 5-6), MSMT-2015 performed well in all scenarios but lost much spatial detail due to coarse resolution. For example, the MSMT-2015 omitted some flat roofs in the suburbs, while in the mountains areas many bare rocks are classified as IS. For GAIA-2018, it keeps good performance in the urban area, but suffers from a severe underestimation problem in suburbs and rural areas. Since GAIA-2018 uses coarse-resolution NLT mask and index-based methods for classification, it can simply and effectively carry out large-scale IS mapping. Still, it missed most rural settlements and sparse impervious objects (row 6, blue ellipses) due to the weak night light intensity and mixed pixels in suburbs and rural areas.

Fig.13 demonstrates the spatial patterns of LMISD-2016, LMISD-2021 and four global IS products in the Lancang-Mekong basin. Notably, GAIA-2018 has less IS area compared to other products, mainly in urban areas along the eastern and southeastern coasts. ESA-2020, MSMT-2015, and our product (LMIS-2016, LMIS-2021) had higher spatial agreement, but the impervious areas of GLC-2017 were smaller in the hinterland of Thailand. Furthermore, our products provide more spatiotemporal dynamic information and finer spatial details of IS. The proposed method has strong performance in identifying small and fragmented impervious objects, such as buildings and roads in villages.

As shown in Figure 14, the four products were scatterplotted against the LMISD impervious maps. The results illustrate a higher consistency between the LMISD-2020 map and ESA-2020 ($R2= 0.97$, $RMSE=4.8\times10\text{-}5$ and slope=0.811) compared to other products. Notably, since GAIA-2018 has been proved to miss some small, fragmented buildings and roads in villages, the regression line in this case has slope less than 1.0 and R2 with lowest value of 0.798. The scatterplot between GLC10-2017 and LMISD-2017 shows a high degree of agreement between GLC10-2017 and LMISD-2017 in “high-fraction” regions (close to 1: 1) but GLC10-2017 was slightly lower than LMISD-2017 over “low-fraction” regions, making the slope of the regression line less than 1. MSMT-2015 has higher IS areas than LMISD-2016, especially for the “low-fraction” regions, indicating that it had an underestimation problem due to limitations of coarse resolution (30m), making the regression slope higher than 1.

https://doi.org/10.5194/essd-2022-251
Preprint. Discussion started: 12 August 2022

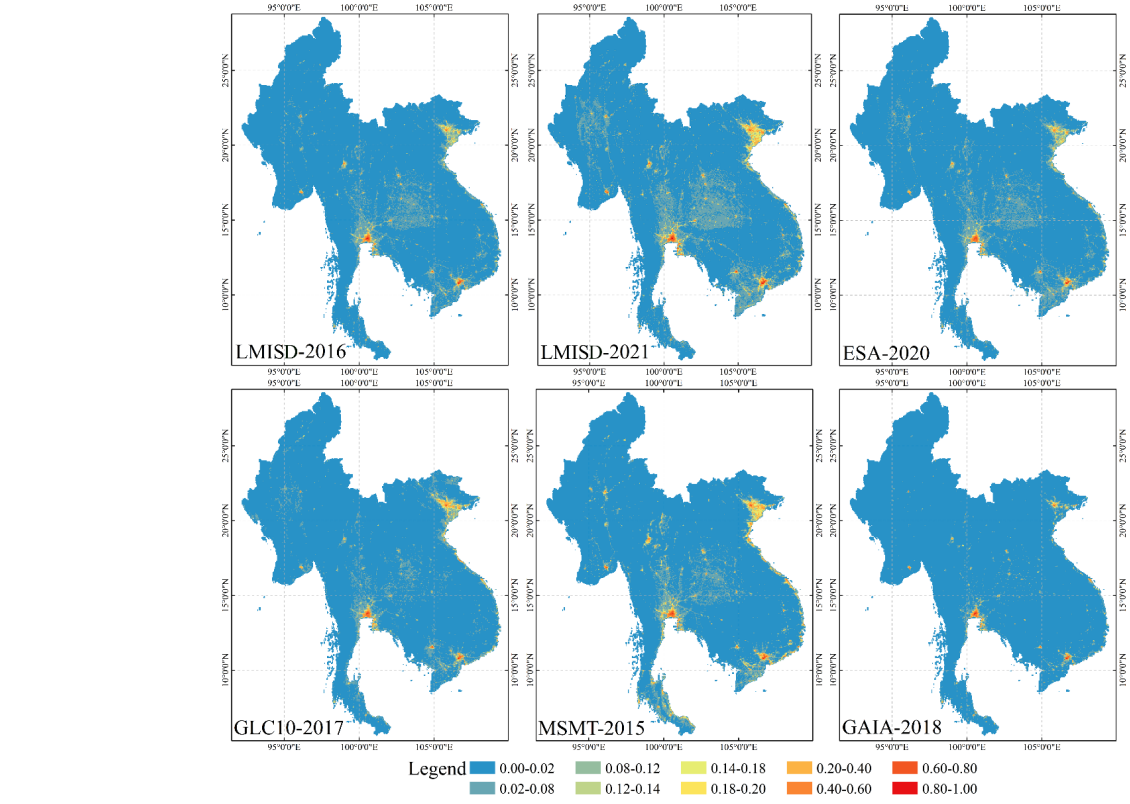

Figure 13: The spatial patterns of five impervious products after aggregating to the grid of 0.05 °×0.05 °. The administrative boundariy was from China Standard Map Service (http://bzdt.ch.mnr.gov.cn/, last access: 15 January 2022).

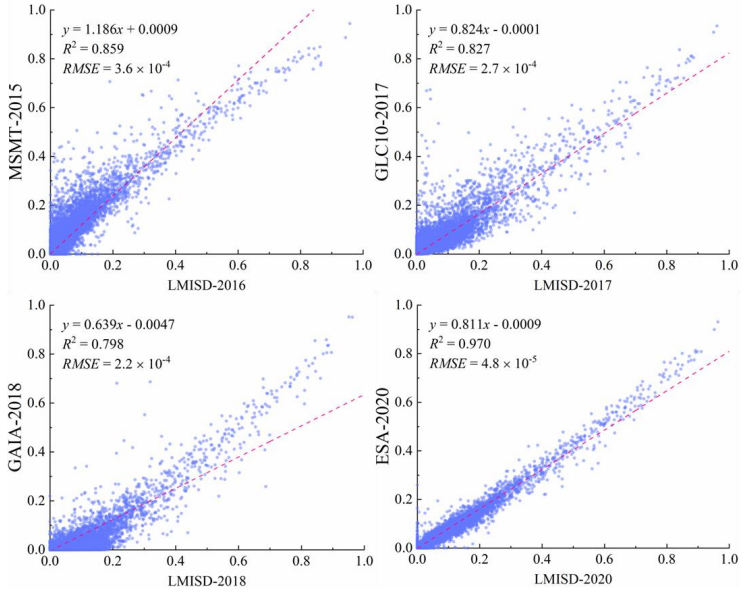

Figure 14: Scatterplots between the LMISD and the MSMT-2015, GLC10-2017, NUACI-2015, and GAIA -2018 global IS products at a spatial grid of 0.05 °×0.05 °.

https://doi.org/10.5194/essd-2022-251
Preprint. Discussion started: 12 August 2022

4.3 Importance analysis of multi-source features

To compare the performance of different feature combinations on IS extraction, the Sentinel-2 optical features classification result was considered as the baseline, adding spectral index, SAR backscattering coefficient, phenological metrics, temporal metrics and GLCM texture to evaluate the OA and Kappa of each group. As shown in Fig.15, the conjunction of the proposed selected SAR features with optical features, performed the best result (final column group), with OA larger than 92% and Kappa larger than 0.82. The results show that multi-source data is beneficial to improving the accuracy of large-scale IS mapping.

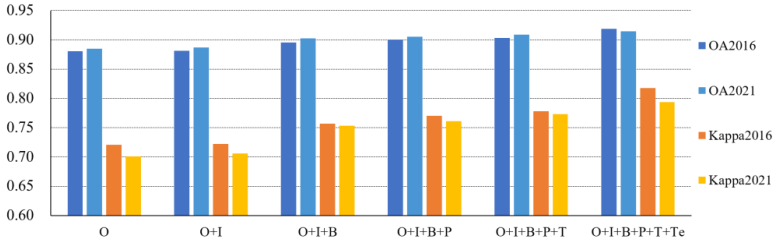

Figure 15: Multi-source feature analysis, O denotes optical data which work as the baseline. I, B, P, T, and Te represent indexes, backscattering, phenology, temporal metrics, and texture features, respectively.

Our research further investigated the importance of all 35 features based on the RF algorithm for IS mapping, which is illustrated in Fig.16. We can conclude that spectral index, spectrum (B2, B11, B12), temporal metrics(VV_stdDev, VH_stdDev), and GLCM texture features (Y_VV_idm, Y_VH_savg, Y_VH_corr) were the four most useful feature groups for IS extraction. The three index metrics (NDVI, NDBI, MNDWI) outperformed in all of the features. In part, this can be explained that the index features highlight the IS from the background, and have a higher spatial resolution (10m) than the other features. Generally, the GLCM texture features derived from SAR images were ranked second, although their importance varies markedly. The importance of temporal features generated from time-series SAR features was inferior to optical features. We found that the phenological features from the SAR data did not show high importance. This is mainly because impervious objects usually remain stable for a short period (e.g., one year) and thus hardly exhibit strong phenological characteristics.

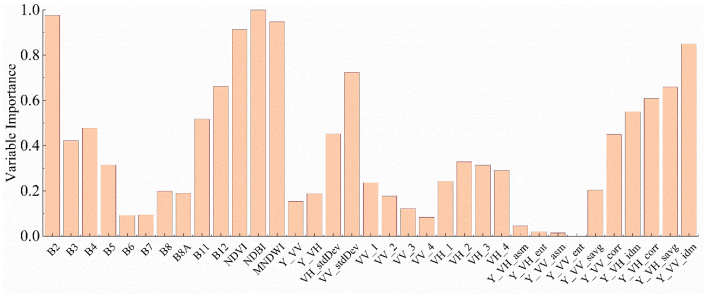

Figure 16: The importance of the input features derived from the random forest model using the training samples

https://doi.org/10.5194/essd-2022-251
Preprint. Discussion started: 12 August 2022

5 Discussion

The fusion of Sentinel-1 and Sentinel-2 data has been used to map IS based on various methods in many previous studies. However, these methods may not be suitable for large-scale, time-series IS mapping in tropical and subtropical areas with cloudy and rainy climates because of the challenges of reference samples, availability of satellite images, and efficient computing equipment. In this paper, a novel framework based on GEE was developed to extract time-series IS with 10-m resolution in the Lancang-Mekong basin by taking advantage of multisource data, sample migration, and temporal consistency checking.

By fully utilizing the the rich spectral information contained in Sentinel-2 imagery and the temporal, texture, and backscatter information obtained from Sentinel-1 imagery, this framework can produce accurate and detailed multitemporal IS maps in varying complex scenarios. First, this framework showed the ability to map IS in the Lancang-Mekong basin, which often impacted the extraction of IS due to cloud cover. More importantly, this framework also performs well in identifying fragmented impervious objects in densely built-up areas, as illustrated in Fig.8. This is because improved spatial resolution can minimize the mixed-pixel phenomenon and provide abundant information in the spatial domain, thus potentially increasing the accuracy and thematic details of IS mapping products (Huang et al., 2018). Moreover, the proposed framework was implemented on the GEE cloud platform, which provides almost all Sentinel-1/2 archive images across the entire time series and study area. The GEE can quickly process large numbers of images in a parallel processing way, regardless of time and space. Therefore, this framework has not only very high computational efficiency but also saves considerable time and space required to download and store data.

Furthermore, the lack of high-quality and abundant train samples seriously hinders producing accurate supervised classification results, especially in large-scale and time-series mapping. It is costly and not practical to collect train samples frequently (e.g., yearly) and consistently. In this study, we utilized Sentinel-2 time-series images to migrate the train samples obtained in the reference year to any target year, effectively reducing the impact of label noise on the accuracy of multiclassification and also facilitating the timely IS mapping for any given year. Additionally, the temporal consistency check method uses temporal context information to correct the binary classification results in detail to generate more reliable multitemporal IS maps.

However, there were also a few limitations that need improved. First. all sample sites were obtained through the manual interpretation of high-resolution Google Earth images to ensure the quantity and quality. Yet, manual interpretation may not be applicable for IS extraction or land cover classification on a larger scale, such as on global scale. Second, many mixed pixels containing both IS and vegetation information may still exist in 10-m resolution images, especially along roads (Yang and Li, 2015; Xu et al., 2018). Thus, pixel-scale methods may omit some small impervious objects, especially in suburban

https://doi.org/10.5194/essd-2022-251
Preprint. Discussion started: 12 August 2022

areas. In the future, we will focus on utilizing crowdsourced geographic data (e.g., OpenStreetMap) and the "soft" classification technique to solve the above problems.

6 Data and Code availability

Our code is publicly available at https://code.earthengine.google.com/74d0845d708a01fde1484c30ca73cc72. And the LMISD was uploaded on https://doi.org/10.5281/zenodo.6968739 (Sun et al., 2022) for free access. It contains a total of 6 bands representing IS distribution maps for 2016, 2017, 2018, 2019, 2020 and 2021. Each band has value 0 for NIS and 1 for IS. This dataset is divided into 69 tiles in GeoTIFF format, named "LMISD-00" to "LMISD-68".

7 Conclusions

In this research, we generated the multitemporal 10-m resolution IS maps in the Lancang-Mekong basin using multisource data, including time-series Sentinel-2, Sentinel-1, and SRTM DEM data. With the integration of multitemporal SAR data, the distinction between IS and other land cover categories can be enhanced compared to using single optical data. Meanwhile, we proposed a sample migration method, which can effectively reduce noise samples to maintain stable accuracy in multitemporal IS mapping. Moreover, the proposed temporal consistency check contributes to improving the accuracy of the multitemporal IS maps by correcting inconsistencies in the initial IS sequence.

The reliability of the annual 10-m resolution IS product has been validated using test samples and compared with four existing global products. The result shows that the OA and Kappa range from 91.45% to 92.44% and 0.829 to 0.848, respectively. As the first attempt to demonstrate the potential applications of this framework, we analyzed the spatiotemporal dynamics of IS at the national scale and in the Lancang-Mekong basin. Results show that a considerable increase in IS area occurs from 2016 to 2021. The total area of IS in 2021 was 37220.27 km^2, which increased by 63% compared to 2016. Thailand has the biggest IS area from 11017.69 km^2 in 2016 to 15927.42 km^2 in 2021. Vietnam has the most significant expansion in IS area with an average growth rate of 831.67 km^2/year

This study provides a multitemporal IS dataset that can serve as a good candidate for urbanization studies in the Lancang-Mekong basin. In the future, other land cover types (e.g., farmlands and forests) will be mapped, not only for IS, to serve the data demand for sustainable development in this region.

Acknowledgments

This work was supported by the National Natural Science Foundation of China (41971292, 41871270, 41801275), and the National Key Research and Development Program (2019YFE0126700).

https://doi.org/10.5194/essd-2022-251
Preprint. Discussion started: 12 August 2022

Reference

Ansari, R. A., Buddhiraju, K. M., and Malhotra, R.: Urban change detection analysis utilizing multiresolution texture features from polarimetric SAR images, Remote Sens. Appl.: Soc. Environ., 20, doi:10.1016/j.rsase.2020.100418, 2020.

Bian, Li, Zuo, Lei, Zhang, and Nan: Estimating 2009–2017 Impervious Surface Change in Gwadar, Pakistan Using the HJ-1A/B Constellation, GF-1/2 Data, and the Random Forest Algorithm, ISPRS Int. J. Geo-Inf., 8, doi:10.3390/ijgi8100443, 2019.

Breiman, L.: Random Forests, Machine Learning, 45, 5-32, doi:10.1023/A:1010933404324, 2001.

Carrasco, L., O'Neil, A., Morton, R., and Rowland, C.: Evaluating Combinations of Temporally Aggregated Sentinel-1, Sentinel-2 and Landsat 8 for Land Cover Mapping with Google Earth Engine, Remote Sens-Basel., 11, doi:10.3390/rs11030288, 2019.

Chen, J., Chen, J., Liao, A., Cao, X., Chen, L., Chen, X., He, C., Han, G., Peng, S., Lu, M., Zhang, W., Tong, X., and Mills, J.: Global land cover mapping at 30m resolution: A POK-based operational approach, ISPRS J. Photogramm. Remote Sens., 103, 7-27, doi:10.1016/j.isprsjprs.2014.09.002, 2015.

Deuskar, C., Baker, J. L., and Mason, D.: East Asia's changing urban landscape: Measuring a decade of spatial growth, World Bank Publications, 2015.

Dong, Y., Ren, Z., Fu, Y., Miao, Z., Yang, R., Sun, Y., and He, X.: Recording Urban Land Dynamic and Its Effects during 2000–2019 at 15-m Resolution by Cloud Computing with Landsat Series, Remote Sens-Basel., 12, doi:10.3390/rs12152451, 2020.

Elvidge, C., Baugh, K., Hobson, V., Kinh, E., Kroehl, H., Davis, E., and Cocero, D.: Satellite inventory of human settlements using nocturnal radiation emissions: a contribution for the global toolchest, Global Change Biol., 3, doi:10.1046/j.1365-2486.1997.00115.x 1997.

Feng, S. and Fan, F.: A Hierarchical Extraction Method of Impervious Surface Based on NDVI Thresholding Integrated With Multispectral and High-Resolution Remote Sensing Imageries, IEEE J. Sel. Top. Appl. Earth Obs. Remote Sens., 12, 1461-1470, doi:10.1109/jstars.2019.2909129, 2019.

Goldblatt, R., Deininger, K., and Hanson, G.: Utilizing publicly available satellite data for urban research: Mapping built-up land cover and land use in Ho Chi Minh City, Vietnam, Dev. Eng., 3, 83-99, doi:10.1016/j.deveng.2018.03.001, 2018.

Gong, P., Li, X., and Zhang, W.: 40-Year (1978–2017) human settlement changes in China reflected by impervious surfaces from satellite remote sensing, Sci. Bull., 64, 756-763, doi:10.1016/j.scib.2019.04.024, 2019a.

Gong, P., Li, X., Wang, J., Bai, Y., Chen, B., Hu, T., Liu, X., Xu, B., Yang, J., Zhang, W., and Zhou, Y.: Annual maps of global artificial impervious area (GAIA) between 1985 and 2018, Remote Sens. Environ., 236, doi:10.1016/j.rse.2019.111510, 2020.

Gong, P., Liu, H., Zhang, M., Li, C., Wang, J., Huang, H., Clinton, N., Ji, L., Li, W., Bai, Y., Chen, B., Xu, B., Zhu, Z., Yuan, C., Ping Suen, H., Guo, J., Xu, N., Li, W., Zhao, Y., Yang, J., Yu, C., Wang, X., Fu, H., Yu, L., Dronova, I., Hui, F., Cheng, X., Shi, X., Xiao, F., Liu, Q., and Song, L.: Stable classification with limited sample: transferring a 30-m resolution sample set collected in 2015 to mapping 10-m resolution global land cover in 2017, Sci. Bull., 64, 370-373, doi:10.1016/j.scib.2019.03.002, 2019b.

Gorelick, N., Hancher, M., Dixon, M., Ilyushchenko, S., Thau, D., and Moore, R.: Google Earth Engine: Planetary-scale geospatial analysis for everyone, Remote Sens. Environ., 202, 18-27, doi:10.1016/j.rse.2017.06.031, 2017.

Grabska, E., Frantz, D., and Ostapowicz, K.: Evaluation of machine learning algorithms for forest stand species mapping using Sentinel-2 imagery and environmental data in the Polish Carpathians, Remote Sens. Environ., 251, doi:10.1016/j.rse.2020.112103, 2020.

Huang, H., Wang, J., Liu, C., Liang, L., Li, C., and Gong, P.: The migration of training samples towards dynamic global land cover mapping, ISPRS J. Photogramm. Remote Sens., 161, 27-36, doi:10.1016/j.isprsjprs.2020.01.010, 2020.

Huang, M., Chen, N., Du, W., Chen, Z., and Gong, J.: DMBLC: An Indirect Urban Impervious Surface Area Extraction Approach by Detecting and Masking Background Land Cover on Google Earth Image, Remote Sens-Basel., 10, doi:10.3390/rs10050766, 2018.

https://doi.org/10.5194/essd-2022-251
Preprint. Discussion started: 12 August 2022

Li, X. and Gong, P.: An "exclusion-inclusion" framework for extracting human settlements in rapidly developing regions of China from Landsat images, Remote Sens. Environ., 186, 286-296, doi:10.1016/j.rse.2016.08.029, 2016.

Li, X., Gong, P., and Liang, L.: A 30-year (1984–2013) record of annual urban dynamics of Beijing City derived from Landsat data, Remote Sens. Environ., 166, 78-90, doi:10.1016/j.rse.2015.06.007, 2015.

Lin, Y., Zhang, H., Lin, H., Gamba, P. E., and Liu, X.: Incorporating synthetic aperture radar and optical images to investigate the annual dynamics of anthropogenic impervious surface at large scale, Remote Sens. Environ., 242, 111757, doi:10.1016/j.rse.2020.111757, 2020.

Liu, C., Zhang, Q., Luo, H., Qi, S., Tao, S., Xu, H., and Yao, Y.: An efficient approach to capture continuous impervious surface dynamics using spatial-temporal rules and dense Landsat time series stacks, Remote Sens. Environ., 229, 114-132, doi:10.1016/j.rse.2019.04.025, 2019.

Liu, D., Chen, N., Zhang, X., Wang, C., and Du, W.: Annual large-scale urban land mapping based on Landsat time series in Google Earth Engine and OpenStreetMap data: A case study in the middle Yangtze River basin, ISPRS J. Photogramm. Remote Sens., 159, 337-351, doi:10.1016/j.isprsjprs.2019.11.021, 2020.

Liu, X., Hu, G., Chen, Y., Li, X., Xu, X., Li, S., Pei, F., and Wang, S.: High-resolution multi-temporal mapping of global urban land using Landsat images based on the Google Earth Engine Platform, Remote Sens. Environ., 209, 227-239, doi:10.1016/j.rse.2018.02.055, 2018.

Markert, K., Schmidt, C., Griffin, R., Flores, A., Poortinga, A., Saah, D., Muench, R., Clinton, N., Chishtie, F., Kityuttachai, K., Someth, P., Anderson, E., Aekakkararungroj, A., and Ganz, D.: Historical and Operational Monitoring of Surface Sediments in the Lower Mekong Basin Using Landsat and Google Earth Engine Cloud Computing, Remote Sens-Basel., 10, doi:10.3390/rs10060909, 2018.

McDonald, R. I., Kareiva, P., and Forman, R. T.: The implications of current and future urbanization for global protected areas and biodiversity conservation, Biol. Conserv., 141, 1695-1703, doi:10.1016/j.biocon.2008.04.025, 2008.

Ngo, K. D., Lechner, A. M., and Vu, T. T.: Land cover mapping of the Mekong Delta to support natural resource management with multi-temporal Sentinel-1A synthetic aperture radar imagery, Remote Sens. Appl.: Soc. Environ., 17, doi:10.1016/j.rsase.2019.100272, 2020.

Nguyen, T. T. H., De Bie, C. A. J. M., Ali, A., Smaling, E. M. A., and Chu, T. H.: Mapping the irrigated rice cropping patterns of the Mekong delta, Vietnam, through hyper-temporal SPOT NDVI image analysis, Int. J. Remote. Sens., 33, 415-434, doi:10.1080/01431161.2010.532826, 2012.

Pesaresi, M., Ehrlich, D., Ferri, S., Florczyk, A., Freire, S., Stamatia, H., Julea, A., Kemper, T., Pierre, S., and Syrris, V.: Operating procedure for the production of the Global Human Settlement Layer from Landsat data of the epochs 1975, 1990, 2000, and 2014, 10.2788/656115, 2016.

Priem, F., Okujeni, A., van der Linden, S., and Canters, F.: Comparing map-based and library-based training approaches for urban land-cover fraction mapping from Sentinel-2 imagery, Int. J. Appl. Earth Obs. Geoinf., 78, 295-305, doi:10.1016/j.jag.2019.02.003, 2019.

Puissant, A., Hirsch, J., and Weber, C.: The utility of texture analysis to improve per-pixel classification for high to very high spatial resolution imagery, Int. J. Remote. Sens., 26, 733-745, doi:10.1080/01431160512331316838, 2005.

Quin, G., Pinel-Puyssegur, B., Nicolas, J.-M., and Loreaux, P.: MIMOSA: An Automatic Change Detection Method for SAR Time Series, IEEE Trans. Geosci., 52, 5349-5363, doi:10.1109/tgrs.2013.2288271, 2014.

Salentinig, A. and Gamba, P.: Combining SAR-Based and Multispectral-Based Extractions to Map Urban Areas at Multiple Spatial Resolutions, IEEE Geosci. Remote Sens. Ma., 3, 100-112, doi:10.1109/mgrs.2015.2430874, 2015.

Schneider, A. and Mertes, C. M.: Expansion and growth in Chinese cities, 1978–2010, Environ. Res. Lett., 9, 024008, doi:10.1088/1748-9326/9/2/024008, 2014.

Schneider, A., Friedl, M. A., and Potere, D.: Mapping global urban areas using MODIS 500-m data: New methods and datasets based on 'urban ecoregions', Remote Sens. Environ., 114, 1733-1746, doi:10.1016/j.rse.2010.03.003, 2010.

https://doi.org/10.5194/essd-2022-251
Preprint. Discussion started: 12 August 2022

575 Shao, Z., Fu, H., Fu, P., and Yin, L.: Mapping Urban Impervious Surface by Fusing Optical and SAR Data at the Decision Level, Remote Sens-Basel., 8, doi:10.3390/rs8110945, 2016.

Slonecker, E. T., Jennings, D. B., and Garofalo, D.: Remote sensing of impervious surfaces: A review, Remote Sensing Reviews, 20, 227-255, doi:10.1080/02757250109532436, 2001.

Song, X.-P., Sexton, J. O., Huang, C., Channan, S., and Townshend, J. R.: Characterizing the magnitude, timing and duration
580 of urban growth from time series of Landsat-based estimates of impervious cover, Remote Sens. Environ., 175, 1-13, doi:10.1016/j.rse.2015.12.027, 2016.

Stehman, S. V. and Foody, G. M.: Key issues in rigorous accuracy assessment of land cover products, Remote Sens. Environ., 231, doi:10.1016/j.rse.2019.05.018, 2019a.

Stehman, S. V. and Foody, G. M.: Key issues in rigorous accuracy assessment of land cover products, Remote Sens. Environ.,
585 231, 111199, doi:10.1016/j.rse.2019.05.018, 2019b.

Sun, G., Li Z., Zhang, A., Wang X., Ding S., Jia X., Li J., and Liu Q.: High-resolution and Multitemporal Impervious Surface Mapping in the Lancang-Mekong Basin with Google Earth Engine , Zenodo [data set], doi: 10.5281/zenodo.6872737, 2022

Sun, Z., Xu, R., Du, W., Wang, L., and Lu, D.: High-Resolution Urban Land Mapping in China from Sentinel 1A/2 Imagery Based on Google Earth Engine, Remote Sens-Basel., 11, 752, doi:10.3390/rs11070752, 2019.

590 Uhlmann, S. and Kiranyaz, S.: Classification of dual- and single polarized SAR images by incorporating visual features, ISPRS J. Photogramm. Remote Sens., 90, 10-22, doi:10.1016/j.isprsjprs.2014.01.005, 2014.

Van De Kerchove, R., Zanaga, D., De Keersmaecker, W., Souverijns, N., Wevers, J., Brockmann, C., Grosu, A., Paccini, A., Cartus, O., and Santoro, M.: ESA WorldCover: Global land cover mapping at 10 m resolution for 2020 based on Sentinel-1 and 2 data, AGU Fall Meeting 2021,

595 Weng, Q.: Remote sensing of impervious surfaces in the urban areas: Requirements, methods, and trends, Remote Sens. Environ., 117, 34-49, doi:10.1016/j.rse.2011.02.030, 2012.

Xu, F., Li, Z., Zhang, S., Huang, N., Quan, Z., Zhang, W., Liu, X., Jiang, X., Pan, J., and Prishchepov, A. V.: Mapping Winter Wheat with Combinations of Temporally Aggregated Sentinel-2 and Landsat-8 Data in Shandong Province, China, Remote Sens-Basel., 12, doi:10.3390/rs12122065, 2020.

600 Xu, H., Wei, Y., Liu, C., Li, X., and Fang, H.: A Scheme for the Long-Term Monitoring of Impervious−Relevant Land Disturbances Using High Frequency Landsat Archives and the Google Earth Engine, Remote Sens-Basel., 11, doi:10.3390/rs11161891, 2019.

Xu, R., Liu, J., and Xu, J.: Extraction of High-Precision Urban Impervious Surfaces from Sentinel-2 Multispectral Imagery via Modified Linear Spectral Mixture Analysis, Sensors-Basel., 18, 2873, doi:10.3390/s18092873, 2018.

605 Yang, J. and Li, P.: Impervious surface extraction in urban areas from high spatial resolution imagery using linear spectral unmixing, Remote Sens. Appl.: Soc. Environ., 1, 61-71, doi:10.1016/j.rsase.2015.06.005, 2015.

Yang, L., Huang, C., Homer, C. G., Wylie, B. K., and Coan, M. J.: An approach for mapping large-area impervious surfaces: synergistic use of Landsat-7 ETM+ and high spatial resolution imagery, Can. J. Remote Sens., 29, 230-240, doi:10.5589/m02-098, 2003.

610 Zeng, Q., Xie, Y., and Liu, K.: Assessment of the patterns of urban land covers and impervious surface areas: A case study of Shenzhen, China, Phys. Chem. Earth., Parts A/B/C, 110, 1-7, doi:10.1016/j.pce.2019.04.002, 2019.

Zhang, H. and Xu, R.: Exploring the optimal integration levels between SAR and optical data for better urban land cover mapping in the Pearl River Delta, Int. J. Appl. Earth Obs. Geoinf., 64, 87-95, doi:10.1016/j.jag.2017.08.013, 2018.

Zhang, H., Lin, H., Li, Y., Zhang, Y., and Fang, C.: Mapping urban impervious surface with dual-polarimetric SAR data: An
615 improved method, Landscape Urban Plan., 151, 55-63, doi:10.1016/j.landurbplan.2016.03.009, 2016.

Zhang, X., Liu, L., Wu, C., Chen, X., Gao, Y., Xie, S., and Zhang, B.: Development of a global 30 m impervious surface map using multisource and multitemporal remote sensing datasets with the Google Earth Engine platform, Earth Syst. Sci. Data., 12, 1625-1648, doi:10.5194/essd-12-1625-2020, 2020.

https://doi.org/10.5194/essd-2022-251
Preprint. Discussion started: 12 August 2022

Zhao, M., Zhou, Y., Li, X., Cheng, W., Zhou, C., Ma, T., Li, M., and Huang, K.: Mapping urban dynamics (1992–2018) in Southeast Asia using consistent nighttime light data from DMSP and VIIRS, Remote Sens. Environ., 248, 111980, doi:10.1016/j.rse.2020.111980, 2020.

Zhu, Z., Zhou, Y., Seto, K. C., Stokes, E. C., Deng, C., Pickett, S. T. A., and Taubenböck, H.: Understanding an urbanizing planet: Strategic directions for remote sensing, Remote Sens. Environ., 228, 164-182, doi:10.1016/j.rse.2019.04.020, 2019.